

# Synchrotron applications of an amorphous silicon flat-panel detector

John H. Lee,<sup>a\*</sup> C. Can Aydiner,<sup>b</sup> Jonathan Almer,<sup>a</sup> Joel Bernier,<sup>a</sup>  
Karena W. Chapman,<sup>a</sup> Peter J. Chupas,<sup>a</sup> Dean Haeffner,<sup>a</sup> Ken Kump,<sup>c</sup>  
Peter L. Lee,<sup>a</sup> Ulrich Lienert,<sup>a</sup> Antonino Miceli<sup>a</sup> and German Vera<sup>c</sup>

<sup>a</sup>XSD Advanced Photon Source, Argonne National Laboratory, Argonne, IL 60439, USA, <sup>b</sup>Los Alamos National Laboratory, Los Alamos, NM 87545, USA, and <sup>c</sup>GE Healthcare, USA.  
E-mail: jlee@aps.anl.gov

A GE Revolution 41RT flat-panel detector (GE 41RT) from GE Healthcare (GE) has been in operation at the Advanced Photon Source for over two years. The detector has an active area of 41 cm × 41 cm with 200 μm × 200 μm pixel size. The nominal working photon energy is around 80 keV. The physical set-up and utility software of the detector system are discussed in this article. The linearity of the detector response was measured at 80.7 keV. The memory effect of the detector element, called lag, was also measured at different exposure times and gain settings. The modulation transfer function was measured in terms of the line-spread function using a 25 μm × 1 cm tungsten slit. The background (dark) signal, the signal that the detector will carry without exposure to X-rays, was measured at three different gain settings and with exposure times of 1 ms to 15 s. The radial geometric flatness of the sensor panel was measured using the diffraction pattern from a CeO<sub>2</sub> powder standard. The large active area and fast data-capturing rate, *i.e.* 8 frames s<sup>-1</sup> in radiography mode, 30 frames s<sup>-1</sup> in fluoroscopy mode, make the GE 41RT one of a kind and very versatile in synchrotron diffraction. The loading behavior of a Cu/Nb multilayer material is used to demonstrate the use of the detector in a strain–stress experiment. Data from the measurement of various samples, amorphous SiO<sub>2</sub> in particular, are presented to show the detector effectiveness in pair distribution function measurements.

**Keywords:** X-ray detector; strain measurement; pair distribution function measurement.

## 1. Introduction

Imaging detectors have been widely used at synchrotron light sources for experiments such as powder diffraction, small-angle scattering and single-crystal diffraction. At photon energies around 20 keV, a charge-coupled device (CCD) camera with optical taper and optical phosphor is one of the most popular detectors. The detector has a low noise level and in the best case scenario the capability of single photon detection. The readout time is of the order of 1 s. In order to obtain a large imaging area and high pixel count, a CCD mosaic is usually used. For example, a 4 × 4 array is implemented in the MAR Research CCD325 (325 mm × 325 mm active area with ~73 μm × 73 μm pixels), and each CCD has its individual taper and measurement circuitry. Owing to the thickness of the phosphor being used, ~40 μm of Gd<sub>2</sub>O<sub>2</sub>S:Tb in CCD325 for example, its efficiency is low at photon energy higher than 20 keV. On the other hand, an image plate (IP) that is made on a monolithic substrate is frequently used with incident photon energy up to about 55 keV. A MAR Research

Mar345 IP has an active area close to 345 mm in diameter with a minimum pixel size around 100 μm × 100 μm. Nevertheless, owing to its serial readout mechanism, the average readout time is about 70 s, which is much longer compared with that of the CCD.

The large detector area with its high pixel count, sensitivity towards high-energy photons, and fast frame rate has made the amorphous silicon (a-Si) detector a very attractive complement to the imaging capability of the CCD and IP. An a-Si detector panel is made on a monolithic glass substrate. Hydrogenated silicon is deposited on the substrate; both the sensor and the thin-film transistor (TFT), which controls the access to the sensor, are made using the deposited materials. The size of the monolithic detector panel can be made to 410 mm × 410 mm. A doped phosphor layer (about several 100 μm) is then deposited directly on top of the sensor array. The nominal incoming photon energy is usually designed to be around 80 keV. The detector does not require a low-temperature cooling system; it only needs a small chiller to keep the sensor panel at room temperature. So the detector

system can be made to be comparably compact. Such a detector is very widely used in medical imaging, *e.g.* in mammography and angiography (Neitzel, 2001; Sivanathan *et al.*, 2004; Spahn, 2005). A video frame rate of 30 frames  $s^{-1}$  is usually available. At present there are two types of flat-panel detector, namely direct and indirect-type. The a-Si panel described is an indirect-type detector. The major difference between the two types of detectors is that in a direct-type detector the conversion layer (or X-ray absorbing layer) is made of photoconductor instead of phosphor. Amorphous selenium (a-Se), about 250  $\mu\text{m}$  to 500  $\mu\text{m}$  thick, is one of the materials used. The incoming X-ray photons are directly turned into electron–hole pairs in the conversion layer and then the resulting charges are swept to the storage capacitor under a static electric field (Chotas *et al.*, 1999). The a-Se detector provides a better modulation transfer function (MTF) performance than the a-Si indirect-type flat-panel detector. On the other hand, the a-Si indirect detector has a higher detective quantum efficiency value at low exposure which will have an advantage in fast frame-rate applications (Albagli *et al.*, 2003).

The Advanced Photon Source (APS) has acquired an a-Si detector system, the GE 41RT from GE. It has been used at the APS for over two years, mainly in the high-energy beamlines 1-ID, 11-ID and 6-ID. The use rate for the detector is close to 100% of the beam time. It has been successfully applied to strain and pair distribution function (PDF) measurements (Aydiner *et al.*, 2007; Bag *et al.*, 2007; Chapman *et al.*, 2006; Michel *et al.*, 2007). These techniques each have their own requirements on the diffracted image. The strain measurement is usually made in low momentum transfer ( $Q$ ). For the PDF method, one usually strives for high spatial resolution in real space, hence measurements need to be performed up to high- $Q$  values, which translates into performing the experiment using high-energy photons, usually in the range 80–100 keV, and requires a detector with a large pixel count.

The subject of this article is examination of the capabilities of the GE 41RT in synchrotron applications. In §2 the set-up of the detector system will be discussed, including some specific software that was developed in order to integrate the system into standard synchrotron beamline operation. In §3 we will discuss some of the detector characteristics that we have measured using a monochromatic X-ray beam from the APS synchrotron light source. Similar measurements are usually carried out using an X-ray tube (Granfors & Aufrichtig, 2000; Granfors *et al.*, 2003; Vedantham *et al.*, 2000; Weisfield *et al.*, 1999) source with an emission spectrum that contains a broad energy background besides the required photon energy. The energy-dependent quantities of the detector can be better measured using a synchrotron light source. Properties such as linearity, responsivity, lag, MTF, dark noise and geometric correction will be discussed. Lag and dark noise are important in measurements that involve a low signal level and a signal that has a wide dynamic range. The MTF is the transfer function of the detector at different spatial frequencies; hence its measurement will give insight into the spatial resolution of

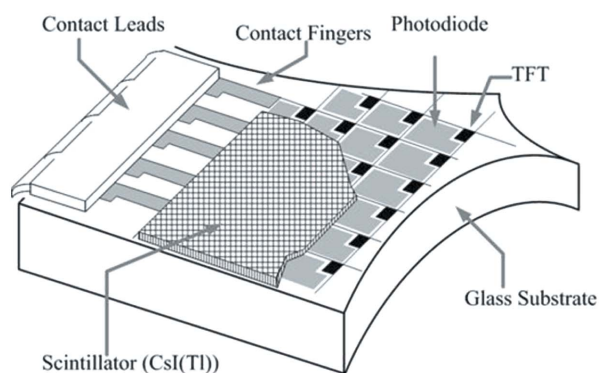
the detector. The geometric flatness of a detector panel is of particular importance to those who are interested in knowing the precise location of various features in a diffraction pattern. For example, in strain measurement, an inherently distorted image may be incorrectly interpreted as strain present in the sample. Without loss of generality, all the characterization measurements are made in the  $2k \times 2k$  mode and at a gain of  $4400 \text{ e ADU}^{-1}$  (electrons per detector count) if not stated otherwise. All image frames are gain-corrected (using the correction program from GE) and background-subtracted before the extraction of required data, except in §3.4 where raw data are used. In §4 we discuss the detector application in strain and PDF measurements. We explain why this detector is suitable for those measurements by looking at some real situation data.

## 2. Detector system

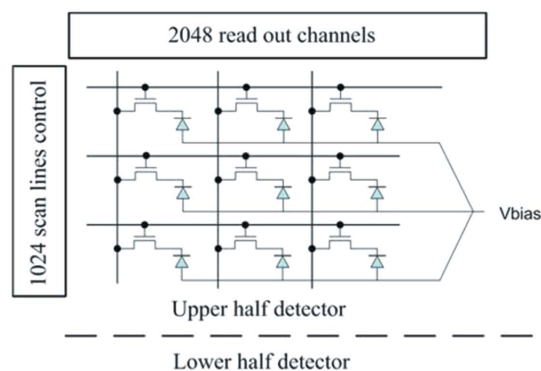
### 2.1. Detector hardware

Amorphous silicon can be deposited on a large glass substrate using a comparatively economical method such as plasma-enhanced chemical vapor deposition. The relatively low cost of manufacturing and the ability to achieve a large active area have made this material a good candidate for large-area microelectronics. Products such as solar cell panels, active-matrix LCD displays and, in particular, flat-panel imaging sensors have been made using the material (Kanicki, 1991). Vendors such as GE, Perkin Elmer, and Varian in the United States; Trixell in Europe; and Canon in Japan have been offering similar imaging systems mainly in the medical and industrial X-ray tomography market. In most imaging applications the active sensor element is a photodiode working in charge storage mode. Charges caused by ionizing radiations are first collected by the active element, and then read out and processed. The a-Si diode offers better radiation resistance than its crystalline silicon counterpart (Perez-Mendez *et al.*, 1987) under the same operating conditions owing to the disordered nature of the parent material.

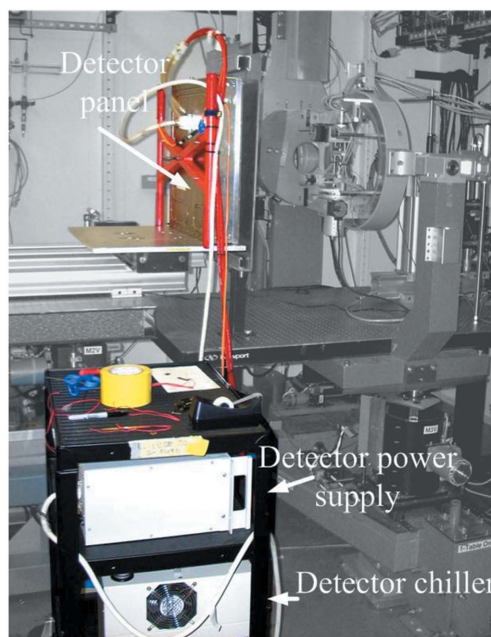
Fig. 1(a) shows the generic layout of a flat-panel sensor array on a glass substrate. In the case of the GE 41RT, the array is composed of  $2048 \times 2048$  a-Si diode elements, and the size of each pixel is  $200 \mu\text{m} \times 200 \mu\text{m}$ . A phosphor layer, usually CsI(Tl),  $\sim 500 \mu\text{m}$  thick, is deposited directly on top of the sensor array. To improve the resolution of the detector, the phosphor material usually possesses a columnar structure. An X-ray photon incident on the phosphor is transformed into visible photons. The visible photons subsequently excite electron–hole pairs in the diode. In the case of ideal operation, before the exposure of a sensor element, its associated storage capacitor is charged to a known voltage. The ionizations caused by incoming photons discharge the capacitor and make the voltage across it drop. The current that is needed to recharge the effective capacitor to its predefined voltage is read out as a signal that is proportional to the incident photon intensity. In reality, the storage capacitor is recharged towards a predefined voltage in a fixed amount of time. This deviation



(a)



(b)



(c)

**Figure 1**

(a) Structure of the detector panel. Amorphous silicon is deposited on a monolithic glass substrate. A photodiode and neighboring TFT form a unit element on the detector sensor array. The CsI(Tl) phosphor is deposited directly on top of the diode array. (b) Matrix addressing readout scheme of the sensor array. The detector is partitioned into two halves, and each half has its own scan line control and column readout circuit. One whole row is read at the same time, and which row is being read at the moment is determined by the scan line control signal. (c) A GE 41RT system is shown in a strain measurement set-up. It consists of a detector sensor panel, a power supply and a chiller.

from the ideal operation contributes to lag which will be investigated in §3.2. The effective storage capacitor usually consists either of the junction capacitor of the a-Si diode or the junction capacitor plus an additional capacitor added in parallel to the diode.

The readout of a flat-panel detector is usually carried out in a matrix-addressing format, as shown in Fig. 1(b). Each sensing pixel consists of a photodiode and a switching thin-film transistor (TFT). When the TFT is turned on, the corresponding diode is connected to the readout circuitry. The readout circuit turns the charging signal of the diode into a voltage signal. Usually a charge-sensitive amplifier carries out the conversion. Each vertical line in the figure is connected to an individual readout circuit that is not part of the sensor array. The readout circuit contains a 14-bit analog-to-digital converter. An entire row of pixels is read out simultaneously. The scan lines determine which row is read at the moment. In the GE 41RT, the whole panel is further divided into two halves. Each half is driven by its own scan line signal and has its own column readout circuits. The detector readout time is independent of the chosen exposure time. Each row of data takes about 124  $\mu\text{s}$  to be read out. Hence it takes 126 ms to read out one whole frame, and 8 frames  $\text{s}^{-1}$  is the maximum frame rate of the detector in  $2\text{k} \times 2\text{k}$  mode. The on resistance of the TFT and the capacitance of the effective storage capacitor determine the primary time constant that limits the reading rate of the detector. When images are continuously acquired, each row covers somewhat shifted time windows. So when a dynamic process with comparable time scale is continuously monitored by the detector, corresponding timing corrections may need to be made on different rows of the captured data frames.

Fig. 1(c) shows the GE 41RT system in a strain measurement set-up. It consists of a flat-panel assembly, a power supply, a very compact chiller and a control computer. The chiller is used to maintain the temperature of the flat-panel detector at 299 K. The control computer is located outside of the experimental hutch and is not shown. It is connected to the detector panel by an optical fiber cable.

## 2.2. Detector software

In the data acquisition application for the synchrotron light source, the GE 41RT communicates, *via* an optical fiber channel (FC), with a control PC (Fig. 2). On the PC, a PCI bus-based proprietary card, the detector framing node (DFN), is used to handle communication with the detector, control image acquisition and perform synchronization with external devices. The PC can be configured to use up to 2.8 GB of memory for images, which is sufficient to acquire 360 images of  $2\text{k} \times 2\text{k}$  pixels in radiography (RAD) mode, or 1440 images of  $1\text{k} \times 1\text{k}$  pixels in fluoroscopy (Angio) mode. The size of the memory will allow continuous data acquisition for 45 s at top speed, 8 frames  $\text{s}^{-1}$ , in the RAD mode and 48 s at top speed, 30 frames  $\text{s}^{-1}$ , in the  $2 \times 2$  binned and  $1\text{k} \times 1\text{k}$  region of interest (ROI) Angio mode. The PC can be fit with a second monitor to display images in real time (as they are received

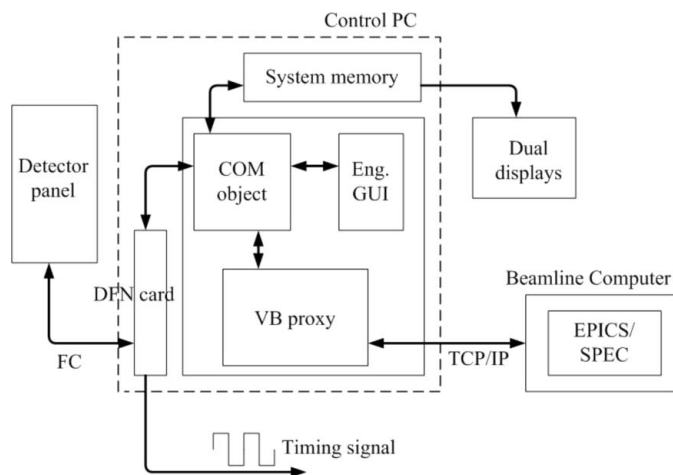


**Figure 2**  
The interconnection of hardware and software of the GE RT41 system.

from the detector). The transfer rate of data from the memory to local disk is about 47 Mbytes s<sup>-1</sup>. That is, it takes about 0.17 s to store one frame.

The PC system, running on Microsoft Windows, is provided with two GE software applications: a graphical user interface, called the Engineering GUI, and a component object model (COM) server with a scriptable interface. Both applications allow the user to configure the detector, perform image acquisition, store and retrieve images from disk, display images and download firmware. The four important configuration parameters of the detector that need to be adjusted during most of the experiments are its mode of operation, the exposure time of each data frame, its gain setting and the number of frames per acquisition. In order to make the system fit into the existing beamline data acquisition scheme, a Visual Basic (VB) server has been written by the APS Beamline Technical Support group. Communicating to EPICS or SPEC through TCP/IP socket, the Visual Basic server acts as a proxy between the Windows-based COM server and the Unix-based EPICS or SPEC, which is the preferred data-capturing software at the synchrotron light source.

Timing signals are available at the output of the DFN card. There are two types of timing signals: a pulse for each frame or a pulse that remains active for the duration of a specified number of frames. The location of the rising and the falling edge of the timing pulses with respect to image readout can be specified. The timing signals are useful in synchronizing the detector with other experimental equipments; for example, they can be used to synchronize X-ray shutter and sample orientation during a continuous  $\omega$  scan.

### 3. Characterization of the detector

#### 3.1. Detector responsivity

The linearity of the response of the detector as a function of incoming X-ray beam intensity was measured using a monochromatic X-ray beam from the high-energy double-crystal monochromator in sector 1-ID of the APS. The beam intensity

was adapted by varying the gap of the undulator and detuning the second monochromator crystal. The beam size used was about 10  $\mu\text{m} \times 10 \mu\text{m}$ . The incoming beam intensity, in terms of photon counts per second, was monitored by a CyberStar (NaI) scintillation detector before it was applied to the GE 41RT. Sufficient monitoring time was allocated to ensure the stability of the beam intensity each time its value was changed. The shaping time for the pulse-shaping amplifier at the output of the scintillation detector was set at 0.5  $\mu\text{s}$ . The scintillation detector, with a 5 mm-thick scintillator, is 99% efficient at 90 keV. The count rate was efficiency corrected, and it was also dead-time corrected using a simple dead-time model (Knoll, 2000),  $N_0 = N_T / (1 + N_T \tau)$ , where  $N_0$  is the measured count rate,  $N_T$  is the true count rate, and  $\tau$  is the inherent dead-time of the scintillation detector ( $\sim 1 \mu\text{s}$ ) (Gog *et al.*, 2001). The maximum photon flux used was around 90000 counts s<sup>-1</sup>. For each beam intensity level the signal in ADU (unit of detector count) of an 11  $\times$  11 pixel area centered at the beam spot on the a-Si detector was integrated, and the background was subtracted. The area was chosen so that the full strength of the incident beam was accounted for. The intensity of the beam was raised until one of the integrated pixels became saturated. Fig. 3 shows a plot of detector response in ADU against the incident photon count at the photon energy of 80.7 keV. A linear fit was performed on the data. The residual value  $R$  is defined as the percentage difference between the measured and the fitted detector response at a corresponding incident photon flux value. The maximum value of  $R$  is about 3%, and its average value over the whole measurement range is 0.77%. The variation of the value of  $R$  is smaller and its value is closer to 0% at higher incident photon flux values.

After measuring the linearity of the response of the detector, the responsivity of the detector at different energies

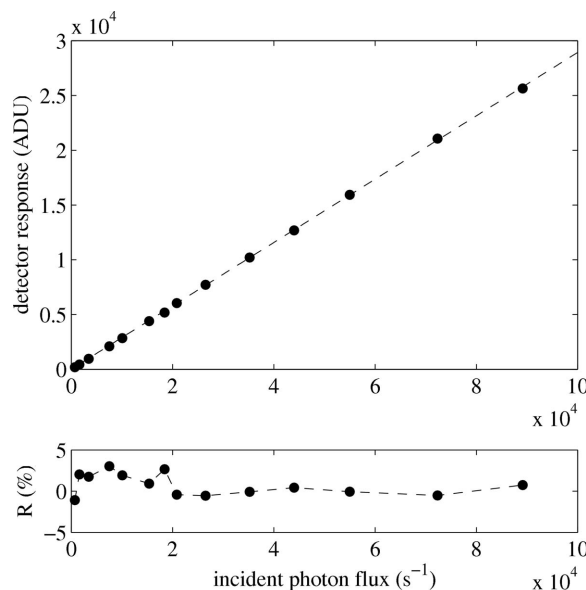


**Figure 3**  
The response of the detector (ADU) versus incident photon flux. The maximum value of  $R$  is about 3% and its average value over the whole measurement range is 0.77%. The dotted line in the upper plot is a linear fit to measured data.

was measured in sector 6-ID. The set-up and method of measurement used was similar to those in the linearity experiment. Instead of beam intensity, the photon energy of the beam was varied. Owing to technical limitations, the X-ray beam size was set to about  $40\ \mu\text{m} \times 40\ \mu\text{m}$ . Beams with photon energy from 30 keV to 90 keV were used. For each photon beam the signal of an  $18 \times 18$  pixel area centered at the beam spot on the detector was integrated. The number of incident photons per second was measured by a CyberStar detector. The responsivity of the a-Si detector in terms of number of photons per ADU was calculated and plotted as a function of energy in Fig. 4. At 79.5 keV the detector responsivity is 3.41 photons per ADU. That is, it takes around three photons to generate one detector count at the detector gain of 4400 e per ADU. The responsivity of the detector varies by 17% from 50 keV to 90 keV, and it deteriorates rapidly with photon energy below 40 keV. At 30 keV the number of photons needed to create one detector count has increased by 69% from its value at 50 keV. The measured responsivity is consistent with that of similar detectors (Street, 2002). The number of charged particles created per absorbed X-ray photon is smaller than that for direct conversion because in this case the responsivity is a product of a number of conversion factors in the signal measurement chain. Factors such as probability of X-ray absorption in the phosphor, scintillation efficiency of the phosphor and the quantum efficiency of the photodiodes all have values less than unity. In particular, the scintillation efficiency of CsI(Tl) is  $\sim 0.15$  (or 15%) (Rocha *et al.*, 2004).

The measured behavior of the responsivity curve can be understood in terms of the efficiency of the detector phosphor layer. The purpose of the phosphor is, first, to capture incoming X-ray photons and, second, to convert the captured X-ray photons into visible photons that the sensors detect. A larger number of visible photons produced will lead to a higher value of detector ADU counts. At the low X-ray photon energy portion of the data shown in Fig. 4, the number of X-ray photons needed to generate 1 ADU increases with

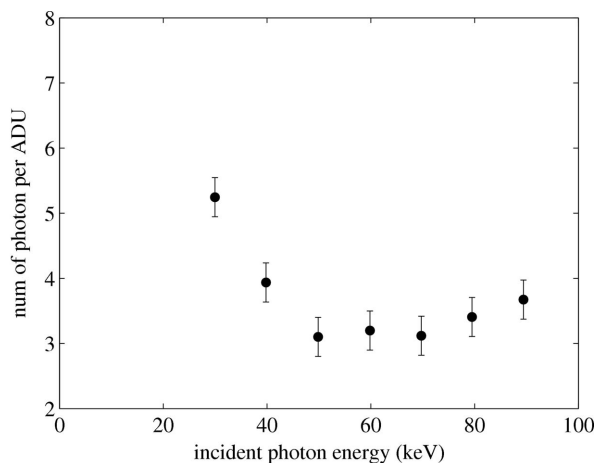


**Figure 4**

The number of photons needed to generate one detector count at different photon energies.

decreasing photon energy because, even though at this energy range the X-ray absorption percentage for the phosphor is high, above 80% (Rocha & Correia, 2001; Rocha *et al.*, 2004), the number of visible photons produced per absorbed X-ray photon decreases with energy. Towards the high-energy end, the responsivity curve rises again owing to the dominating effect of the degradation of the phosphor absorption power with increasing X-ray photon energy.

An important consideration related to the percentage of X-ray absorption of the phosphor is that a 500 mm-thick CsI(Tl) layer absorbs about 50% of 80 keV photons (Ramos *et al.*, 2003); the rest of the X-ray photons will pass through the phosphor layer. An advantage of amorphous silicon diodes is that they are very radiation tolerant compared with single-crystalline silicon sensors. This is because they are very thin and they have an amorphous structure. The fact that they are thin means that direct absorption of X-rays is extremely rare. Furthermore, the amorphous structure is very radiation hard, *i.e.* absorption of X-rays does not disrupt the structure as happens in single-crystalline sensors. Also, in the detector studied, the electronics behind the diode array are shielded by lead which prevents damage to the electronics. For these reasons the detector is not susceptible to noise caused by direct conversion in the sensors and also not damaged by radiation that penetrates the CsI. The amount of noise added by X-rays hitting the sensors and electronics was found to be negligible. The detector has been operating at the APS for two years in the X-ray energy range 50–100 keV with no noticeable deterioration in its performance.

### 3.2. Lag

Lag is the term used to describe the existence of residual signal from a previous exposure. It behaves like forward temporal cross talk between data frames taken at different times (Albagli *et al.*, 2005). It affects the data analysis process when the contrast range of the captured image is wide. The lag artifact from a strong signal region of a previous frame will interfere with the weak signal region of subsequent images. The problem is more severe in the fast-frame-rate mode, where a large number of data frames have to be taken in a short period of time. The conventional way of minimizing the lag during experiments is to take a number of dark frames (frames that have no X-ray exposure) between data frames. There are several contributing factors for lag. In the short time scale, usually the first couple of reads of the detector, the finite charging time of the storage capacitance of the sensor during readout is the dominating factor. It is mainly caused by the RC time constant of the storage capacitor (C) and the finite resistance of the TFT conduction channel (R). At a particular RC value, the longer the charging time allowed, the smaller the size of the lag; however, long charging (read) time will compromise the frame rate. In general, the read time is set to be around five times the RC value (Maolinbay *et al.*, 2000) so that the pixel signal can be adequately sampled and lag lessened. The afterglow of the scintillator and the de-trapping of charge carriers in the diode will contribute to lag at longer

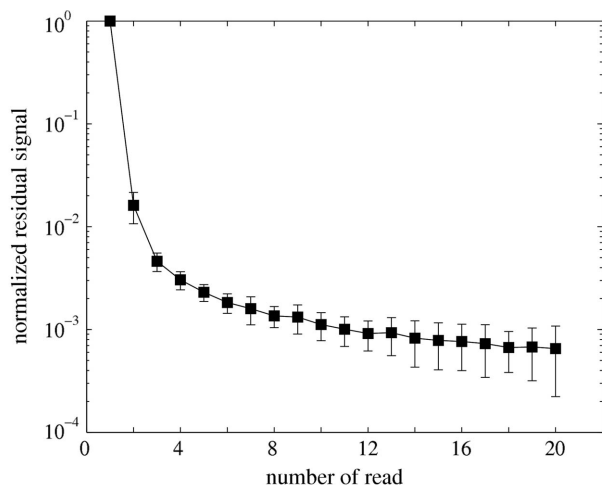


**Figure 5**  
The normalized residual signal with different exposure times was averaged and plotted against the number of reads on the detector. The decay of the normalized signal in the dark frames of various data sets (with different exposure times) is found to follow a general trend as shown by the solid line in the figure, and they are within the error bar provided. The signal drops to 2% of its initial value at the second read and to 0.4% at the third read.

time scales. It is important to note that the read time for a detector is fixed and independent of the exposure time of the detector. It determines the maximum frame rate achievable by the detector.

In order to study the lag behavior of the detector, we have used the diffraction pattern of polycrystalline Cu. The polycrystal was illuminated with an 88.5 keV X-ray beam. The beam shutter was opened for 0.2 s, and then the first frame (data frame that contained the diffraction image) was read. Dark frames were then read with the shutter closed. The data frame and subsequent dark frames constituted a data set. Various data sets were made using different exposure times, namely 0.5 s, 1 s and 10 s, for up to 200 frames in a set.

The intensity of the diffraction pattern in the captured frames within a data set decreased from the first frame on. The decay of the signal, *i.e.* the residual signal, was monitored at each successive frame. The residual signal was normalized to its initial value. The normalized residual signal for different exposure times was averaged and is plotted *versus* the number of reads in Fig. 5. The decay of the normalized signal in the dark frames of various data sets (with different exposure times) is found to follow a general trend as shown by the solid line in Fig. 5, and they are within the error bar provided in the figure. Judging from the data, the signal level of the detector decays to about 2% of its initial value in the second read and to about 0.4% in the third read.

### 3.3. Modulation transfer function

The resolution of an imaging detector is usually expressed in the form of the MTF, which can be found from the spatial Fourier transform of the physical line-spread function (LSF). Flood field images were made at photon energies of 68.80 keV

and 24.21 keV by fluorescence from gold and indium foil, respectively. The same set-up was used for the LSF measurement by placing a 25  $\mu\text{m}$ -wide and 1 cm-long tungsten slit in front of the detector. The long side of the slit was placed at a very shallow angle with respect to the column orientation of the detector sensor array, so that, at a length of 1 cm, the slit would intersect a large number of pixels. In this case it was around 50. The data used for constructing the LSF were then extracted as described by Fujita *et al.* (1992). The LSF of the detector at the two measurement energies are shown in Fig. 6. The LSFs are identical for the two energies. The full width at half-maximum (FWHM) of the LSF is 0.22 mm corresponding to 1.1 pixels. The corresponding MTF is plotted in Fig. 7. The 0.22 mm resolution with  $\sim 500 \mu\text{m}$ -thick phosphor indicates that the columnar structure is indeed effective; however, the lateral spread of light in the phosphor still remains the major contribution to the spatial resolution of the detector.

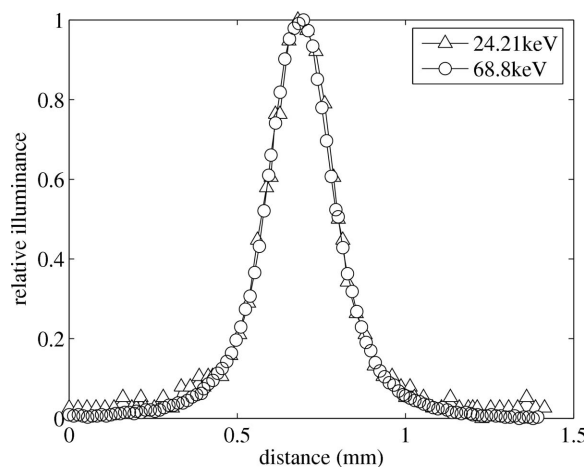


**Figure 6**  
The LSF of the detector at 24.21 keV and 68.80 keV. The form of the LSF is the same at the two energies.

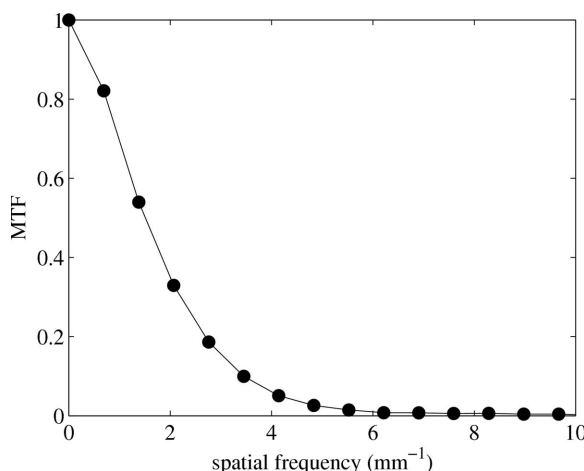


**Figure 7**  
The MTF of the detector is obtained by a spatial Fourier transform of the LSF.

### 3.4. Background (dark) signal and noise

Knowledge of the nature and magnitude of the dark signal is important in understanding the limitation of the performance of the detector at low signal level. Dark frames of different 'exposure times' were taken with three different gains, namely 1100, 2200 and 4400 e ADU<sup>-1</sup>. The exposure time was varied from 1 ms to 15 s. A sequence of ten data frames was taken for each gain and exposure time. The ten frames were averaged to form an averaged frame. The mean pixel value of the averaged frame was used to represent the dark signal. The dark signal at different gain settings is plotted against exposure time in Fig. 8(a). The ten data frames were then subtracted from the averaged frame to calculate ten difference frames. The standard deviations of the ten difference frames were then averaged. The averaged standard deviations are plotted in Fig. 8(b). The corresponding value represents the magnitude of the background noise of the measurement. The noise value obtained using the present method is slightly smaller than that in using the method of taking two images, calculating the standard deviation of the difference image and dividing it by root 2. Nevertheless,

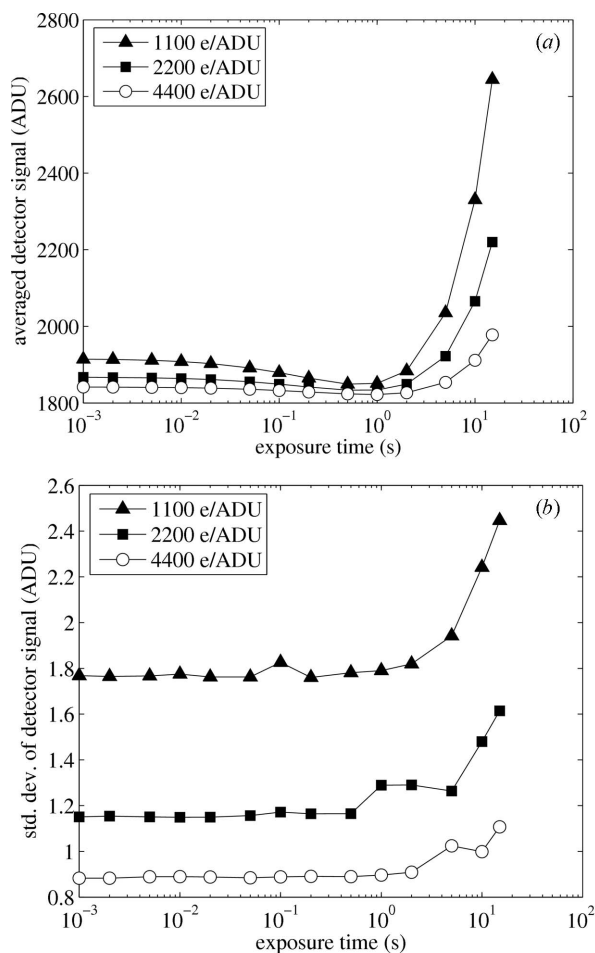


**Figure 8**  
(a) The average dark signal (per pixel) is plotted against different exposure times at different gain settings. (b) The standard deviation of the detector dark signal is plotted against different exposure times at different gain settings.

the difference in the values obtained by the two methods is below 6%.

Before the exposure time of around 1 s, the dark signal is a decreasing function of exposure time, and the percentage difference between its largest and smallest value for each gain setting is about 1%: it is around 1840 ADU for the gain of 4400 e ADU<sup>-1</sup>, 1865 ADU for the gain of 2200 e ADU<sup>-1</sup>, and 1910 ADU for the gain of 1100 e ADU<sup>-1</sup>. For longer exposure times the dark signal is an increasing function of time. With a gain of 1100 e ADU<sup>-1</sup>, the dark signal level rises about 42% when the exposure time is changed from 1 s to 15 s. A possible explanation of the observed dark signal behavior was given by Maolinbay *et al.* (2000). In their model the dark signal included contributions from (a) the TFT switching transient current, (b) leakage current of the photodiode sensor and the TFT (Street, 1991), and (c) charges from the pre-amplification circuit. The switching transient current (a) is a slight decreasing function of exposure time and is the dominating dark-signal factor for short exposure times. The leakage current of the photodiode sensor and the TFT (b) becomes important for longer exposure times. For this detector it appears that the dark signal changes from transient current dominant to leakage current dominant at around 1 s.

With exposure times shorter than 1 s, the background noises in Fig. 8(b) are around 0.9, 1.2 and 1.8 ADU for gain settings of 4400 e ADU<sup>-1</sup>, 2200 e ADU<sup>-1</sup> and 1100 e ADU<sup>-1</sup>, respectively. Similar to the behavior of the dark signal, the size of the background noise rises comparatively faster after 1 s. In the gentler region of the curve, the background noise shown in Fig. 8(b) is believed to be dominated by TFT thermal noise, and at exposure times longer than 1 s it is mainly due to the shot and the 1/f noise of the leakage current of the TFT and the sensor diode (Maolinbay *et al.*, 2000). Owing to the fact that we have dark signal, background subtraction is necessary in experiments with low signal levels. To perform background subtraction correctly, the dark frames used for such subtractions should be taken at the same gain setting and exposure time as that of the data frames.

### 3.5. Geometric correction

The accurate measurement of distances in the output images is critically dependent on quantifying any inherent spatial distortion. Experimental applications that are particularly sensitive to precise position measurements include structure determination and strain analysis for (poly)crystalline materials. In these data the radial distance from the transmitted beam position to a diffraction line is related to the spacing of specific crystallographic planes; hence quantifying the radial component of the distortion is of primary importance. In this context, azimuthal distortions are of second-order importance and, as a result, are not treated here.

The radial component of the spatial distortion for the flat-panel detector was measured using a single powder-diffraction image. The sample consisted of CeO<sub>2</sub> powder placed in a spinner disc with an effective thickness of ~500 μm. The instrument was configured for a high-energy low-*Q* measure-

**Table 1**

Instrument parameters.

Column 3 shows the initial value of the parameters, and column 4 shows their final value.

Parameter	Description	Initial value	Final value
$\lambda$	X-ray wavelength	0.15380 Å	0.15380 Å
$x_0$	Horizontal pattern center	204.43 mm	204.41 mm
$y_0$	Vertical pattern center	204.88 mm	204.92 mm
$D$	Sample-to-detector distance	1778.44 mm	1777.86 mm
$\gamma_y$	Horizontal tilt angle	0.26°	0.34°
$\gamma_x$	Vertical tilt angle	0.32°	0.54°

ment, which is typical for strain analysis. The minimum observable  $d$ -spacing in this configuration was  $\sim 1.35$  Å. The detector was aligned such that the transmitted beam roughly intersected the center of the active area. All relevant instrument parameters from the measurement are listed in Table 1.

The raw image, shown in Fig. 9(a), was re-binned into polar coordinates (1300 radial and 24 azimuthal bins) using an estimated pattern center. Each 15°-wide azimuthal bin yielded a one-dimensional radial intensity spectrum that was associated with its mean azimuthal position, as shown in Fig. 9(b). An analytic profile function was then fit to each one-dimensional spectrum to estimate the radial positions of the diffraction lines.

Because the CeO<sub>2</sub> is strain free, the geometry of conic sections may be used to relate the azimuthally dependent line positions to the coordinates of the pattern center, tilt of the detector surface, and sample-to-detector distance. The predicted line positions may be obtained from the (known) X-ray wavelength and lattice parameter for CeO<sub>2</sub>. The geometric parameters were refined using a constrained opti-

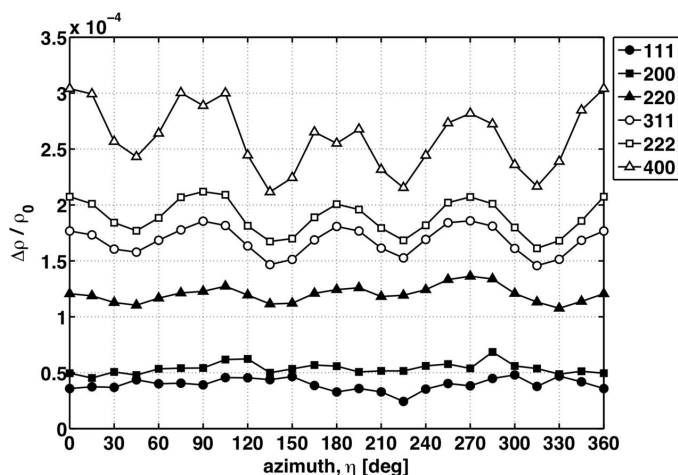


**Figure 10**

The residual discrepancies between the predicted and measured diffraction line positions for CeO<sub>2</sub> following optimization of the geometric parameters alone. The side legend indicates the index of each diffraction line shown in Fig. 9(b). The values for  $\rho_0$  were calculated from the instrument parameters and reference lattice parameter for CeO<sub>2</sub>. The 90° azimuthal periodicity of the radial distortion is evident, as is the radial dependence of its amplitude and offset.

mization scheme to minimize the misfit between the predicted and measured diffraction line positions.

After optimization of the instrument geometry parameters, any residual systematic discrepancies,  $\Delta\rho$ , between the predicted and measured radial positions for each diffraction line are due to radial distortion in the underlying image. These distortions are shown in Fig. 10.

The salient features of the radial distortion field are, first, a 90° azimuthal periodicity, and, second, a monotonically

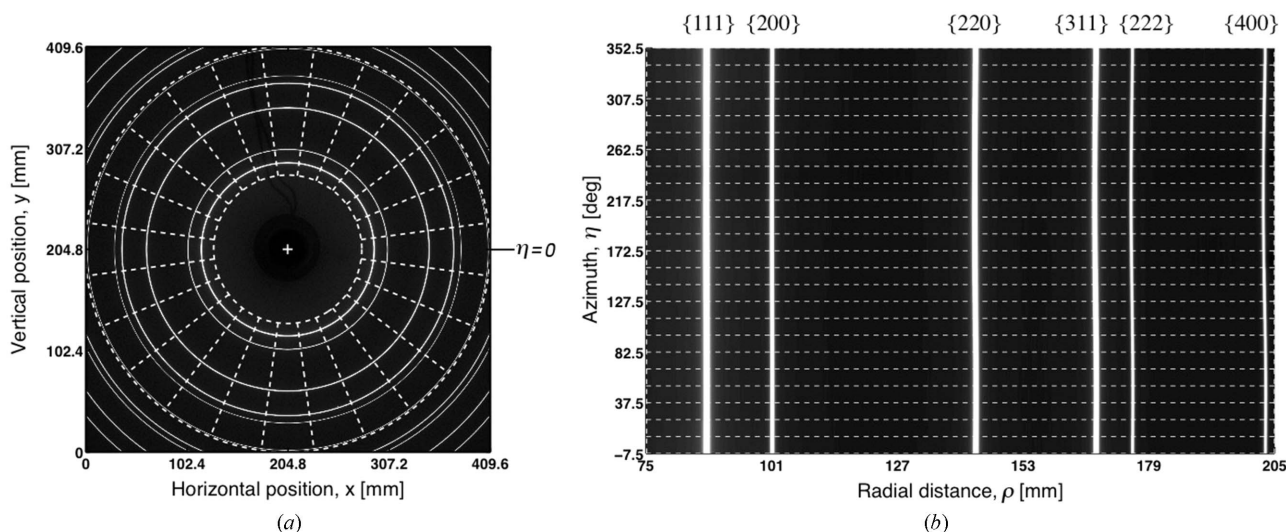


**Figure 9**

(a) A full 2048 × 2048 diffraction image of the CeO<sub>2</sub> calibration standard. The dashed white lines indicate the radial limits and 15° azimuthal sector boundaries used for polar re-binning. (b) The re-binned image using 1000 × 24 (radial × azimuthal) bins and initial instrument parameters obtained from FIT2D. The dashed white lines again indicate the azimuthal bin boundaries. The deviations in the radial positions of the labeled diffraction lines as a function of  $\eta$ , most visible in {222} and {400}, arise primarily from errors in the initial pattern center and tilt angle estimates used in the re-binning process. While radial distortion also contributes to such deviations, the magnitudes under consideration here are imperceptible at this scale.

**Table 2**  
Refined parameters for the distortion function [equation (1)].

Parameter	Value
$a_1$	$-3.174 \times 10^{-5}$
$a_2$	$-2.595 \times 10^{-4}$
$n_1$	3.111
$n_2$	2.295

increasing radial dependence of the amplitude. The average magnitude of the normalized residual discrepancies ( $\Delta\rho/\rho_0$ ) is  $\sim 2 \times 10^{-4}$ , where  $\rho_0$  is the mean radial position for each ideal diffraction line. The value is larger than the typical desired accuracy for strain measurements of  $\sim 1 \times 10^{-4}$ .

Based upon these observations, the following function is proposed for re-scaling the radial axis,

$$f(\rho, \eta) = a_1(\rho/\rho_d)^{n_1} \cos 4\eta + a_2(\rho/\rho_d)^{n_2} + 1, \quad (1)$$

where  $a_1$ ,  $a_2$ ,  $n_1$  and  $n_2$  are scalar parameters;  $\rho_d$  is a reference radius (here  $\rho_d = 204.8$  mm); and the ‘undistorted’ radius  $\hat{\rho}$  is obtained as  $\hat{\rho} \equiv f\rho$ . While the distortion parameters  $a_1$ ,  $a_2$ ,  $n_1$  and  $n_2$  could be estimated directly from the measured radial distortions, this was not the approach taken. Owing to the correlations between the geometric parameters listed in Table 1 and the distortion parameters, the optimization procedure to estimate the geometric parameters was performed again using (1) to calculate  $\hat{\rho}$ ; in this way the distortion parameters were refined simultaneously with the geometric parameters in the nine-dimension solution space. The optimal results for the distortion parameters are listed in Table 2.

The effectiveness of applying this field is shown empirically in Fig. 11. The radial distortions are reduced to a mean value of zero with no discernible systematic behavior. Its overall magnitude is below  $2 \times 10^{-5}$ .

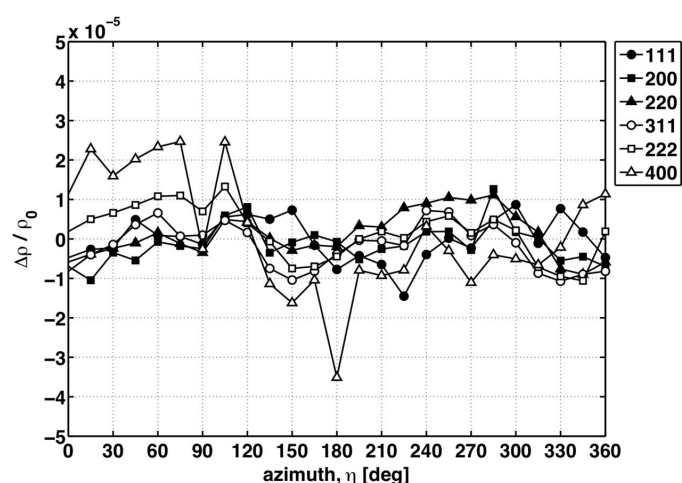


**Figure 11**  
The residual errors in the radial positions of points along the indicated diffraction lines following geometric corrections and radial re-scaling. The mean amplitude is  $\sim 1 \times 10^{-5}$  and the systematic behavior observed in Fig. 10 has been removed.

## 4. Applications

### 4.1. Strain measurements

Metallic multilayers are novel materials that are produced by depositing alternating layers of two different metals by physical vapor deposition where the layer thickness can be controlled down to 1 nm. The mechanical behavior of these materials, when the layer thickness is reduced to the nanometer scale, has received significant attention for two reasons: (i) a very pronounced increase in strength ( $\sim 2$  GPa), and (ii) the alteration of plasticity mechanisms (Misra & Kung, 2001). In particular, at the tens of nanometers scale, single dislocations bowing inside the layer become the active mechanism (Misra *et al.*, 2002, 2005). Here, we investigated the strain rate dependence of these mechanisms in Cu/Nb multilayers with 27 nm layer thickness using synchrotron X-rays.

Diffraction with monochromatic high-energy (80.715 keV) X-rays was used to investigate the residual strains in a Cu/Nb sample (Noyan & Cohen, 1987). The experiment was performed at the 1-ID beamline at APS. The beam size was  $200 \mu\text{m} \times 200 \mu\text{m}$ , and the diffraction volume engulfed of the order of  $10^9$  grains for both Cu and Nb. The Bragg angles are very small ( $1.5\text{--}5^\circ$ ) owing to the X-ray energy used. This allowed entire diffraction rings to be captured on the GE area detector with  $2048 \times 2048$  pixel resolution and  $200 \mu\text{m}$  pixel size. A relatively long detector-to-sample distance ( $D$ ) of 1440 mm was selected for high strain resolution. At this distance the detector encompassed Nb (110), (200), (211) and Cu (111), (200), (220) reflections. Fig. 12 shows the images recorded on the area detector. In addition to Cu and Nb rings, the images contain rings from  $\text{CeO}_2$ , a National Institute of Standard and Technology (NIST) powder standard, applied as a thin layer on the surface of the sample. On this particular sample orientation, reflections from all the encompassed Nb planes and the Cu (220) plane were observed.

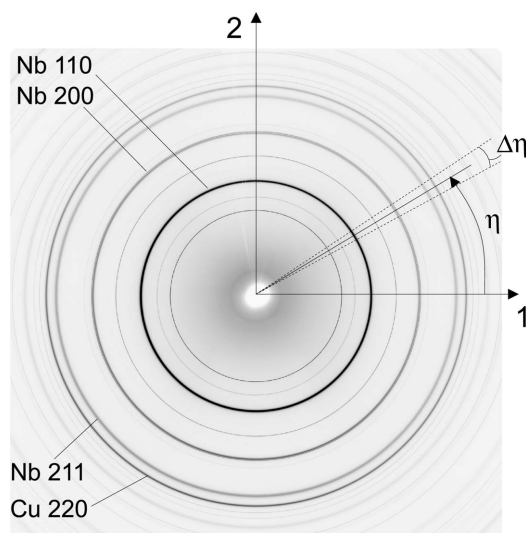


**Figure 12**  
Diffraction image of Cu/Nb multilayers with 27 nm layer thickness. The azimuthal angle  $\eta$ , integration interval  $\Delta\eta$  and reflection rings are shown in the figure. The unlabeled rings inside the Cu 220 ring are due to the thin layer of  $\text{CeO}_2$  standard on the surface of the sample.

Strain along each diffracting plane normal is obtained through the measurement of radius  $r$  at the corresponding azimuth  $\eta$  on the detector. The first step of the numerical procedure is to integrate  $\Delta\eta$  slices (shown in Fig. 12) into one-dimensional intensity ( $I$ ) versus  $r$  patterns for a fixed  $\eta$ . Here,  $\Delta\eta$  was selected as  $5^\circ$  resulting in 72 one-dimensional patterns, and the integration was performed by the *FIT2D* (Hammersley, 1997) program. The peaks in the one-dimensional patterns are then fit with a pseudo-Voigt distribution to yield position, intensity and width of the peaks.

Subsequently, by the iterative calling of the above procedure, the position results for the strain-free  $\text{CeO}_2$  peaks are used to precisely compute the beam center, detector tilt and sample-to-detector distance ( $D$ ). The accuracy of these values is imperative for strain resolution with high-energy X-rays.

Following the internal standard corrections, the position of Cu/Nb peaks is converted to the Bragg angle using  $\theta = (1/2)\tan^{-1}(r/D)$ , and the  $d$ -spacing can be determined by inserting  $\theta$  into the Bragg condition  $\lambda = 2d\sin\theta$ . Then, strain is given by

$$\varepsilon = (d - d_0)/d_0, \quad (2)$$

where  $d_0$  is the strain-free  $d$ -spacing. Here, we are particularly interested in the  $\eta = 90^\circ$  data, which obtains its signal from atomic planes whose normal (under small  $\theta$  assumption) is the tensile-loading direction.

Although synchrotrons are extremely brilliant, the time scale of the observed events has been limited by detector response time (frame rate). In particular, *in situ* loading experiments have been limited to quasi-static strain rates with a stepwise loading scheme where the sample is kept under a constant load for tens of seconds while data are acquired. With the new GE detector, strain rates up to  $10^{-2} \text{ s}^{-1}$  under continuous loading become available. This strain rate is still moderately low (1% strain is attained in 1 s) compared with, for example, Hopkinson bar experiments; yet, if the material is strain-rate sensitive in the  $10^{-5}$ – $10^{-2} \text{ s}^{-1}$  range, much more information about the nature of deformation behavior is captured with diffraction that is phase and atomic plane resolved. Here, we successfully collect and reduce diffraction strain data at 5 Hz as the sample is tensile-loaded continuously at a strain rate of  $0.7 \times 10^{-2} \text{ s}^{-1}$ . Fig. 13 plots average stress versus tensile-direction lattice strains in representative reflections of Nb (110) and Cu (220), for both a quasi-static stepwise loading and the  $0.7 \times 10^{-2} \text{ s}^{-1}$  strain rate. The deviation from linearity in these curves that initiates around 400 MPa, where Cu and Nb curves bend left and right, respectively, demonstrates load transfer from Cu to Nb grains. This means Cu grains yield and start to lose their capacity to take further load, which would show in their lattice strains. The observed plasticity happens exactly the same way for both strain rates. Although we observed no noticeable strain-rate sensitivity in this case, this experiment proves the concept and makes experiments on actual strain-rate-sensitive materials at the  $\sim 10^{-2} \text{ s}^{-1}$  level a new and interesting field.

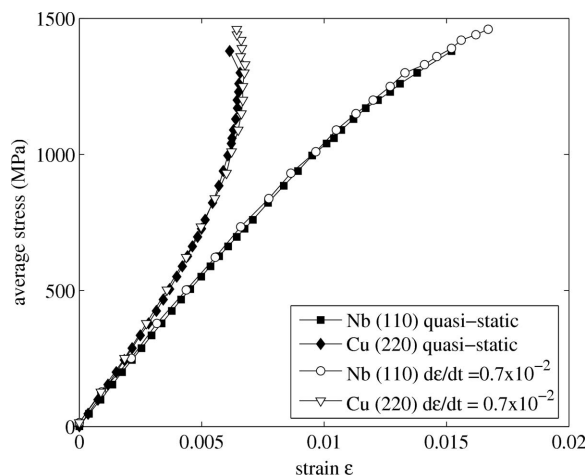


**Figure 13** Average stress of the Cu/Nb multilayer is plotted against its tensile direction lattice strains in representative reflections of Nb (110) and Cu (220) for both quasi-static stepwise loading and  $0.7 \times 10^{-2} \text{ s}^{-1}$  strain rate.

#### 4.2. PDF measurements using the a-Si detector

The atomic PDF has become the method of choice for characterizing the atomic scale structure of disordered and amorphous materials. The PDF technique recovers structural information in the form of a distribution of atomic distances,  $r$ , and thus does not rely on the assumption of translational invariance that traditional crystallographic methods apply. A key experimental criterion for obtaining quantitative PDFs,  $G(r)$ , is to be able to measure the total structure function  $S(Q)$  to large values of momentum transfer with sufficient statistics to adequately correct for Compton scattering. The term  $S(Q)$  is related to the elastic part of the total diffracted intensity  $I^{\text{el}}(Q)$  by the formula (Warren, 1990)

$$S(Q) = 1 + \frac{[I^{\text{el}}(Q) - \sum c_i |f_i(Q)|^2]}{\sum |c_i f_i(Q)|^2}, \quad (3)$$

where  $c_i$  and  $f_i$  are the atomic concentration and scattering factor, respectively, for the atomic species of type  $i$ , and  $Q$  is defined as  $4\pi\sin\theta/\lambda$ . The angle between the incidence and scattered wavevector is  $2\theta$ , and  $\lambda$  is the wavelength of the incidence photon.

The PDF is obtained experimentally by direct Fourier transformation of the total structure factor  $S(Q)$  by the relation

$$G(r) = (2/\pi) \int_{Q=0}^{Q_{\text{max}}} Q[S(Q) - 1] \sin(Qr) dQ. \quad (4)$$

The PDF is defined as  $G(r) = 4\pi r[\rho(r) - \rho_0]$ , where  $\rho(r)$  is the local atomic number density, and  $\rho_0$  is the average atomic number density. It probes the probability of finding two atoms separated by a distance  $r$  (*i.e.* atom–atom correlations), including those that may deviate from the average long-range structure. Based on total scattering data, which include Bragg diffraction and the diffuse contribution arising from disordered features, PDF methods are particularly valuable in the structural analysis of nanoscale and disordered (crystalline

and non-crystalline) systems, for example, glass, liquid, amorphous, nanocrystalline, heterogeneous and crystalline materials.

The preferred present approach for obtaining moderate-resolution X-ray PDF measurements ( $Q_{\max} \approx 20\text{--}25 \text{ \AA}^{-1}$ ) is based on the ‘rapid acquisition’ (RA-PDF) methodology, which combines high-energy X-rays ( $>50 \text{ keV}$ ) with large-area detectors (typically imaging plates/IPs) to allow the simultaneous measurement of the scattering intensity to high-momentum transfers (Chupas *et al.*, 2003, 2007). This approach collects all data simultaneously; however, it does not allow for direct discrimination of Compton scattering at large values of  $Q$ . This offers a considerable improvement over the traditional point-by-point scanning approach, reducing data collection times for PDF analysis from hours to minutes. However, despite continual advances in X-ray beam properties, higher-resolution X-ray PDFs ( $Q_{\max} > 35 \text{ \AA}^{-1}$ ) and fast time-resolved PDF measurements ( $<2 \text{ min}$  intervals) are still ultimately limited by the properties of the IP detector. In contrast to conventional area detectors such as IPs, typically used at moderate X-ray energies ( $\sim 20 \text{ keV}$ ), the GE flat-panel detector is optimized for the detection of high-energy X-rays, 80–100 keV, owing to its originally intended applications in medical imaging. Furthermore, it has a large active area ( $410 \text{ mm} \times 410 \text{ mm}$ ), improved effective detector resolution, virtually continuous data accumulation, and fast readout capabilities (up to 8 or 30 Hz), properties advantageous for quantitative high-energy X-ray scattering measurements for PDF analysis using area detectors.

We have examined the capabilities of the detector for measuring PDF data on a variety of amorphous and crystalline samples. Fig. 14 shows an example of  $S(Q)$  and  $F(Q)$ , where  $F(Q) = Q[S(Q) - 1]$ , obtained for amorphous  $\text{SiO}_2$ . These data were collected to high values of momentum transfer by averaging several hundred images together. While X-ray data measured using single-point counters and solid-state detectors have taken on the order of 12–24 h to measure weakly scattering samples such as  $\text{SiO}_2$  (Petkov *et al.*, 2000), the data in

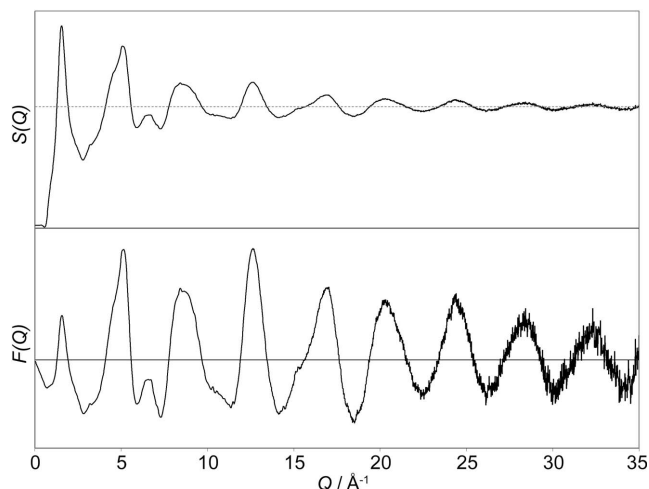


**Figure 14**  
 $S(Q)$  and  $F(Q)$  for amorphous  $\text{SiO}_2$ .

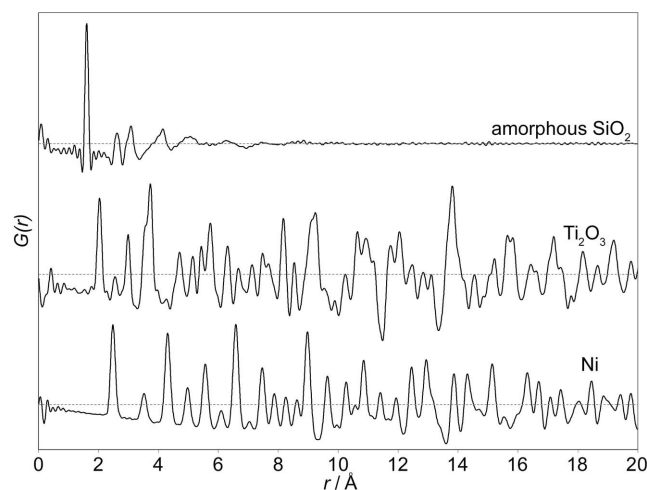


**Figure 15**  
 $G(r)$  shown for  $\text{SiO}_2$ ,  $\text{Ti}_2\text{O}_3$  and Ni, obtained from the Fourier transform of  $F(Q)$ , measured to a  $Q_{\max}$  of 35, 35 and 40  $\text{\AA}^{-1}$ , respectively.

Fig. 14 demonstrate the possibility of collecting data in the time range of several minutes. However, it is important to note that such measurements in the future will benefit from the availability of Compton scattering corrections that make use of the type of data shown in Fig. 4. The response of the GE detector is significantly more uniform over energies above 60 keV than that of the image plates (Jakoncic *et al.*, 2006). Compton scattering makes up  $\sim 98\%$  of the signal of  $\text{SiO}_2$ , and convolution with the data in Fig. 4 will improve the quality of the PDFs extracted from the raw diffraction data. The PDFs given in Fig. 15 show high-quality data that can be obtained from the detector. The lack of any large peaks in the low- $r$  region ( $<1 \text{ \AA}$ ) is an indication of the quality of the data. Any modulation occurring as a long-wavelength modulation in  $F(Q)$ , as would occur with systematic errors, would cause spikes in the low- $r$  region of  $G(r)$ .

Preliminary measurements of representative crystalline and amorphous samples have shown that, in addition to producing X-ray PDFs of generally high quality, the a-Si detector has a number of distinct advantages for PDF measurements: the improved real-space resolution allowed by the large active area can enable atomic correlations of similar length to be distinguished; the fast readout and enhanced sensitivity can enable previously unfeasible time-resolved PDF experiments; and the exceptional signal-to-noise ratio available with the high sensitivity coupled with the ability to continuously accumulate data over an extended time period can allow extremely small relative contributions, such as from a weak or highly dilute feature, to be reliably measured.

## 5. Conclusions

We have examined a number of operational characteristics of the GE 41RT a-Si flat-panel detector. The detector response is linear before saturation in the operational photon energy of 80.7 keV. The FWHM of the LSF is 1.1 pixels. The detector signal lag is 2% of its original signal in the second read and

drops to about 0.4% at the third read. A correction formula has been proposed to minimize the systematic radial distortion of the detector. From studying the experimental data taken using the detector, its fast frame rate and large active area with high pixel count have opened up new opportunities for dynamics measurements in both strain and PDF measurements at the nominal energy of about 80 keV.

We thank Dr Paul R. Granfors of GE Healthcare for his advice on the article. Use of the Advanced Photon Source was supported by the US Department of Energy, Office of Science, Office of Basic Energy Sciences, under contract No. DE-AC02-06CH11357.

## References

- Albagli, D., Han, S., Couture, A., Hudspeth, H., Collazo, C. & Granfors, P. (2005). *Proc. SPIE*, **5745**, 1078–1086.
- Albagli, D., Hudspeth, H., Possin, G., Lee, J., Granfors, P. & Giambattista, B. (2003). *Proc. SPIE*, **5030**, 553–563.
- Aydiner, C. C., Brown, D. W., Misra, A., Mara, N. A., Wang, Y.-C., Wall, J. J. & Almer, J. (2007). *J. Appl. Phys.* **102**, 083514.
- Bag, S., Trikalitis, P. N., Chupas, P. J., Armatas, G. S. & Kanatzidis, M. G. (2007). *Science*, **317**, 490–493.
- Chapman, K. W., Chupas, P. J., Maxey, E. R. & Richardson, J. W. (2006). *Chem. Commun.* pp. 4013–4015.
- Chotas, H. G., Dobbins, J. T. & Ravin, C. E. (1999). *Radiography*, **210**, 595–599.
- Chupas, P. J., Chapman, K. W. & Lee, P. L. (2007). *J. Appl. Cryst.* **40**, 463–470.
- Chupas, P. J., Qiu, X., Hanson, J. C., Lee, P. L., Grey, C. P. & Billinge, S. J. L. (2003). *J. Appl. Cryst.* **36**, 1342–1347.
- Fujita, H., Tsai, D. Y., Itoh, T., Doi, K., Morishita, J., Ueda, K. & Ohtsuka, A. (1992). *IEEE Trans. Med. Imag.* **11**, 34–39.
- Gog, T., Venkataraman, C. & Casa, D. M. (2001). Private communication.
- Granfors, P. R. & Aufrichtig, R. (2000). *Med. Phys.* **27**, 1324–1331.
- Granfors, P. R., Aufrichtig, R., Possin, G. E., Giambattista, B. W., Huang, Z. S., Liu, J. & Ma, B. (2003). *Med. Phys.* **30**, 2715–2726.
- Hammersley, A. P. (1997). *FIT2D: An Introduction and Overview*. ESRF Internal Report ESRF97HA02T. ESRF, Grenoble, France.
- Jakoncic, J., Di Michiel, M., Zhong, Z., Honkimaki, V., Jouanneau, Y. & Stojanoff, V. (2006). *J. Appl. Cryst.* **39**, 831–841.
- Kanicki, J. (1991). *Amorphous and Microcrystalline Semiconductor Devices: Optoelectronic Devices*. Boston: Artech House.
- Knoll, G. F. (2000). *Radiation Detection and Measurement*. New York: John Wiley and Sons.
- Maolinbay, M., El-Mohri, Y., Antonuk, L. E., Jee, K.-W., Nassif, S., Rong, X. & Zhao, Q. (2000). *Med. Phys.* **27**, 1841–1854.
- Michel, F. M., Ehm, L., Antao, S. M., Lee, P. L., Chupas, P. J., Liu, G., Strongin, D. R., Schoonen, M. A. A., Phillips, B. L. & Parize, J. B. (2007). *Science*, **316**, 1726–1729.
- Misra, A., Hirth, J. P. & Hoagland, R. G. (2005). *Acta Mater.* **53**, 4817–4824.
- Misra, A., Hirth, J. P. & Kung, H. (2002). *Philos. Mag. A*, **82**, 2935–2951.
- Misra, A. & Kung, H. (2001). *Adv. Eng. Mater.* **3**, 217–222.
- Neitzel, U. (2001). *Medicamundi*, **45**, 8–13.
- Noyan, I. C. & Cohen, J. B. (1987). *Residual Stress: Measurement by Diffraction and Interpretation*. New York: Springer.
- Perez-Mendez, V., Kaplan, S. N., Ward, W., Qureshi, S. & Street, R. A. (1987). *Nucl. Instrum. Methods Phys. Res. A*, **260**, 195–200.
- Petkov, V., Billinge, S. J. L., Sashtri, S. & Himmel, B. (2000). *Phys. Rev. Lett.* **85**, 3436–3439.
- Ramos, N. F., Rocha, J. G., Lancers-Mendez, S., Wolffenbuttel, R. F. & Correia, J. H. (2003). *Proc. Eurosensors XVII*, pp. 208–209.
- Rocha, J. G. & Correia, J. H. (2001). *Sens. Actuators A*, **92**, 203–207.
- Rocha, J. G., Ramos, N. F., Lancers-Mendez, S., Wolffenbuttel, R. F. & Correia, J. H. (2004). *Sens. Actuators A*, **110**, 119–123.
- Sivananthan, M. U., Moore, J., Cowan, J. C., Pepper, C. B., Hunter, S., Cowen, A. R., Davies, A. G. & Kengyelics, S. M. (2004). *Medicamundi*, **48**, 2–10.
- Spahn, M. (2005). *Medicamundi*, **15**, 1934–1947.
- Street, R. A. (1991). *Philos. Mag. B*, **63**, 1343–1363.
- Street, R. A. (2002). *APS News*, **11**, 6.
- Vedantham, S., Karellas, A., Suryanarayanan, S., Albagli, D., Han, S., Tkaczyk, E. J., Landberg, C. E., Opsahl-Ong, B., Granfors, P. R., Lewis, I., D’Orsi, C. J. & Hendrick, R. E. (2000). *Med. Phys.* **27**, 558–567.
- Warren, B. E. (1990). *X-ray Diffraction*. New York: Dover.
- Weisfield, R. L., Hartney, M. A., Schneider, R., Aflatooni, K. & Lujan, R. (1999). *Proc. SPIE*, **3659**, 307–317.